Nanoscale

Melamine-Graphene Epoxy Nanocomposite Based Die Attach Films for Advanced 3D Semiconductor Packaging Applications

Journal:	*Nanoscale*
Manuscript ID	NR-ART-08-2022-004557
Article Type:	Paper
Date Submitted by the Author:	20-Aug-2022
Complete List of Authors:	Sun, Zhijian; Georgia Institute of Technology, ; Wong, Ryan; GAtech Liu, Yifan; GAtech Yu, Michael; GAtech Li, Jiaxiong; Georgia Institute of Technology College of Engineering Spence, Daron; Oak Ridge National Laboratory, ; Georgia Institute of Technology College of Engineering, Zhang, Mingyue; GAtech Kathaperumal, Mohanalingam; GAtech Wong, Ching Ping; Georgia Institute of Technology, Materials Science and Engineering; Chinese University of Hong Kong,

Melamine-Graphene Epoxy Nanocomposite Based Die Attach Films for Advanced 3D Semiconductor Packaging Applications

Zhijian Sun[a], Ryan Wong[a], Yifan Liu[a], Michael Yu[a], Jiaxiong Li[a], Daron Spence[a], Mingyue Zhang[a], Mohanalingam Kathaperumal[b], Ching-Ping Wong[a*]

[a] School of Materials Science and Engineering, Georgia Institute of Technology, Atlanta, Georgia 30332, United States.

[b] School of Electrical and Computing Engineering, Georgia Institute of Technology, Atlanta, Georgia 30332, United States.

Corresponding author: cp.wong@mse.gatech.edu (C.P. Wong)

Abstract

With the ultra-fast development of personal portable electronic devices, it is important to explore new die attach film (DAF) materials in the limited mounting area and height in order to meet the requirements of a high packaging density and a high operating speed. Graphene-based epoxy nanocomposites are becoming one of the most promising candidates for the next generation of DAFs combining the ultra-high thermal conductivity of graphene, and ultra-strong adhesion of epoxy polymers. However, poor dispersion and weak interfacial connections, due to the overly smooth surface of graphene nanosheets, are still pressing issues that limit their industrial applications. Additionally, pristine graphene nanosheets have only a small effect on improving the glass transition temperature (T_g) of epoxy composites to meet the requirements of DAFs. In this work, melamine-functionalized graphene is synthesized by using a nondestructive ball milling process, which results in greater dispersion and enhancement of the interfacial connections between graphene and epoxy resins demonstrated by both experimental and simulation results. In particular, the aromatic triazine rings of melamine increase T_g in the cured resin, thus improving the thermal stability of DAFs.

The melamine-graphene (M-G) epoxy nanocomposites synthesized have a high T_g of 172°C and an out-of-plane thermal conductivity of 1.08 W/mK at 10 wt% loading. This is 6.4 multiples higher than that of neat epoxy. Moreover, M-G epoxy nanocomposites exhibit superb thermal stability, an effective low coefficient of thermal expansion (CTE), low moisture adsorption, and a useful high electrical resistivity. In the DAF

performance test, involving experimentation and modeling, the samples present a better cooling capability and heat dissipation. This supports the idea that our findings have potential to be applied in the next generation of DAFs for high-power and high-density 3D packaging.

1 Introduction

Recently, advanced semiconductor encapsulation become one of the most important technologies due to the rapid development and high demand for personal portable electronic devices.[1,2] The excelling performance of these devices requires a high packaging density and a high operating speed in the limited mounting area and height.[3,4] Thus, stacked multi-chip packages (Stacked-MCP) were developed for satisfying the stringent requirements of these smaller, thinner, and high-performance electronic devices such as mobile phones, tablets, and laptops.[5,6] Within the Stacked-MCP, System in Package (SiP) has emerged and well developed, because it combines the different functions of dies, logic, and memory stacked in a package to meet the demand of the miniaturization of electronic devices, where the multi-die stack-ups are interconnected by through silicon via (TSV) vertical interconnections.[7,8] TSV can provide excellent electrical interconnection and small footprint in 3D packages with high reliability and performance.[9,10] During the system integration process, die attach materials have been widely employed when dies are stacked with substrate or other dies to reach a larger capacity in 3D SiP. Traditionally, silver flakes-filled epoxy as die-attach adhesives have been used in between dies and substrates in lead-frame-based packages because they provide uniform and controllable interconnections.[11] However, they only show high thermal conductivity only at ultrahigh filler loadings because silver itself has a lower thermal conductivity than graphene of around 429 W/mK. At high filler loadings, it causes the epoxy composite to be brittle, which can cause reliability issues such as failure in the drop test. Also, a high filler loading

results in epoxy composites with a high storage modulus. If the moduli are too high, the thermal stresses will be high in the interface. This causes more reliability problems for semiconductor packaging applications. So, researchers recently have been working on combining silver fillers with other types of fillers to achieve high thermal conductivity at a lower filler loading to solve the above issues (Table S1). Moreover, silver paste easily causes package cracking or delamination during reflow soldering, and it also has wettability and processability issues in high integration and high pin counts packages.[12] Overall, silver-epoxy paste struggles with thermal conductivity, processability, reliability, etc. Thus, die attach films (DAFs) have been introduced and became more popular recently due to its lack of not only voids, but also its absence of paste bleeding and slanting.[11,13-16]

The requirements of DAFs in modern high density 3D electronic packages include low heat resistance, high adhesion strength, high glass transition temperature (T_g), and low coefficient of thermal expansion (CTE).[11,17-21] Epoxy resins as the matrix of polymer composites have already been applied in DAF vendors such as Henkel and AI Technology for several years because epoxy resins have many hydroxyl groups after curing, which provide strong adhesion strength between the die and substrate. However, epoxy itself has a low thermal conductivity (only around 0.2 W/mK), which will cause high thermal resistance between the chip and substrate.[22,23] Thus, nanofillers need to be added to epoxy in order to achieve high thermal conductivity and low thermal resistance. Among many fillers, graphene nanosheets are the top candidates for next generation of DAFs because of their excellent thermal

conductivity (3500–5300 W/mK) and high surface area (~2630 m^2/g).[24–26] Their monatomic 2-D sp^2 hybridized structure creates an efficient heat transport path.[27] Many graphene-based epoxy composites have already been reported to achieve high thermal conductivity.[28–30] However, due to the overly smooth surface of graphene nanosheets, poor dispersion and weak interfacial connections are still large issues that limit their industrial applications.[31,32] Additionally, pristine graphene nanosheets only have a small effect on improving the T_g of epoxy composites to meet the requirements of DAFs.[33,34] Therefore, it is a major challenge to create graphene-based epoxy DAFs with both high through-plane thermal conductivity and high T_g under a reasonable curing schedule.

In this work, melamine functionalized graphene has been fabricated by using a nondestructive ball milling process. The sp^2 hybridized conjugated structure of melamine provides π−π stacking interactions with graphene nanosheets, which result in better dispersion without creating any defects on the surface of graphene. Moreover, the amine groups of melamine open the epoxide groups and enhance the interfacial connections with epoxy resins. In particular, the aromatic triazine rings of melamine could provide a high T_g in the cured resin to improve the thermal stability of DAFs. The resultant epoxy nanocomposites presented a high through-plane thermal conductivity of 1.08 W/mK at 10 wt% filler loading and a high T_g of 172 °C under a curing schedule of 155 °C for 90 mins. Additionally, they also present a low CTE, low moisture adsorption and effective electric resistivity. Compared to silver-epoxy pastes, our work shows improvements in thermal conductivity, processability, CTE,

and thermal stability and represents an advanced in the die attach materials field in the application of 3D semiconductor packaging. Meanwhile, to emulate epoxy nanocomposites in real world applications, they have been used and modeled as DAFs. Heat and time-based experiments and thermal simulations have revealed important features of these epoxy nanocomposites as DAFs. These results provide new insights into the design and fabrication of graphene-based epoxy nanocomposites to meet the needs of next-generation DAF in high density 3D electronic packaging.

2 Results and Discussion

2.1 Preparation and characterization, and simulation of the melamine functionalized graphene:

The preparation procedure of the synthesis of melamine functionalized graphene is illustrated in Figure 1a. The melamine was mixed with graphene nanosheets using a nondestructive ball milling process. The morphology of graphene nanosheets after functionalization is shown in scanning electron microscopy (SEM), transmission electron microscopy (TEM) and optical microscopy (OM) images. The pristine graphene nanosheets have a mean diameter of around 1 μm, and they showed semi-transparency through TEM characterizations (Figure 1b-c and S1a-e), indicating the thinness of graphene nanosheets. Atomic force microscopy (AFM) also indicated the low thickness of graphene nanosheets to be around 21 nm (Figure 1d-e). After functionalization, the surface of melamine-graphene (M-G) became rougher and coarser, and the thickness of melamine-graphene increased to 65 nm (Figure 1f-g, 2a and S1f-h), which indicates that the melamine attached on the surface of graphene

successfully. Moreover, the graphene nanosheets were more obscure in Figure 2b and S1f when treated with melamine due to the amorphous organic layer coating. At the same time, the graphene flakes with a lateral size of around 50 μm also co-exist with graphene nanosheets, which facilitate the formation of a thermal transport internetwork.

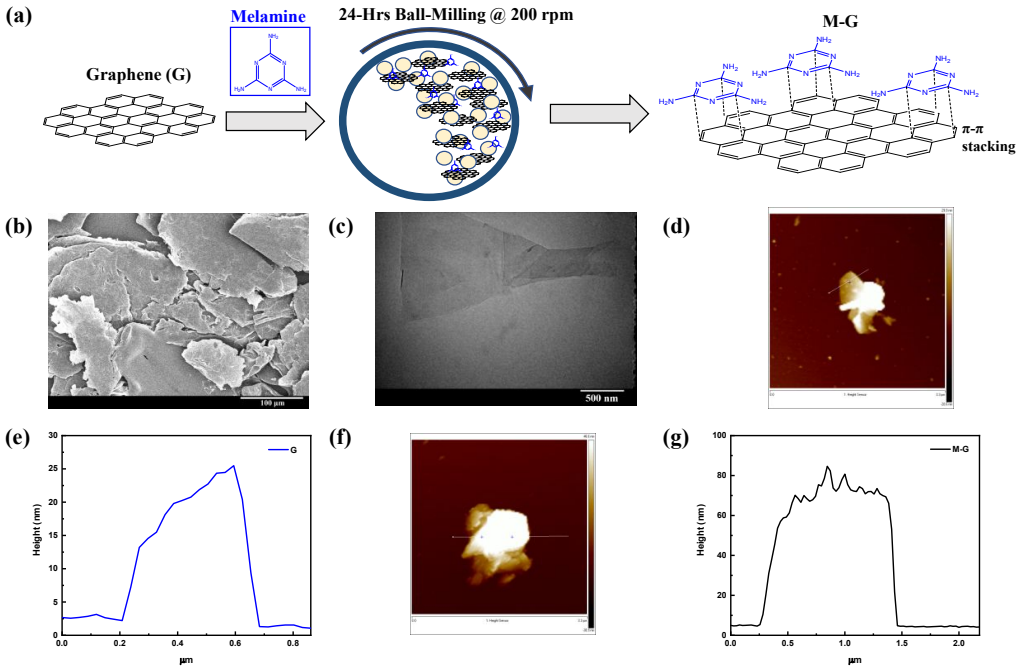

Figure 1. (a) Schematic of the synthesis process. (b) SEM image, (c) TEM image and (d) AFM image of graphene nanosheets. (e) The height of graphene nanosheets. (f) AFM image of M-G. (g) The height of M-G.

To further confirm the interaction between melamine and graphene, X-ray photoelectron spectroscopy (XPS), Fourier-transform infrared spectroscopy (FTIR), and thermogravimetric analysis (TGA), Raman and X-ray diffraction (XRD) were utilized. The XPS elemental analysis and survey curve (Figure S2a-b) identified the appearance of nitrogen in M-G, showing how melamine and G connected. The C 1s

XPS spectrum of M-G in Figure 2c was separated into five major peaks with binding energies at 284.5, 286.0, 287.6, and 290.5 eV, corresponding to C-C, C-N and C-O, C=N and C=O, and π−π satellite components, respectively.[35] The appearance of C-N and C=N peaks at 286.0 and 287.6 eV, respectively, supports that melamine has attached with graphene nanosheets. The deconvolution of the N 1s XPS spectrum in Figure S2c reveals three peaks at 398.4 (neutral imine), 399.1 (neutral amine), and 400.1 eV (charged nitrogen), also indicating a connection between melamine and graphene by π−π bonds.[36,37] FTIR results in Figure 2d show that M-G has characteristic peaks around 3200 cm^{-1} due to N-H stretching vibrations and characteristic peaks around 1500 cm^{-1} due to C–N and C=N stretching vibrations. Moreover, the breathing mode of s-triazine rings cause several peaks around 900 cm^{-1}.[38–40] These results help prove that melamine attached to the graphene. In Figure 2e, the TGA of M-G composite also provides evidence of noncovalent functionalization of graphene with melamine. The M-G exhibits weight loss between pristine graphene and pure melamine, which shows residual weight of 53.9% at 800 °C. Melamine degraded quickly, only around 260°C due to the low thermal stability of organic molecules. Raman spectroscopy (Figure 2f) shows that the characteristic peaks of G and M-G can be found near 1345 (D-band), 1576 (G-band), and 2720 cm^{-1} (2D-band). For pristine graphene, the exhibited G-band/2D-band ratio of 1.92 reveals that few-layer graphene is present.[41] After functionalization, the 2D-band of M-G was slightly shifted, resulting in a 10 cm^{-1} down-shift compared to pristine graphene (2720 cm^{-1}).[42] A low D-band to G-band ratio means negligible damage caused by the

modifications, and the ratio found for the M-G samples was 0.22. Thus, melamine modifications caused insignificant damage to the graphene nanosheets. These results all suggest that melamine successfully connected with graphene via π-π interactions.[43] In addition, for XRD as shown in Figure 2g, the high intensity of diffraction peaks at 26.60° can be assigned to the (002) plane of graphene nanosheets, indicating high crystallinity of both G and M-G nanosheets. In addition, the claims that melamine functionalization does not affect the crystal structure of graphene and that melamine is amorphous are supported by the fact that G and M-G share the same characteristic diffraction peaks after 20°. Otherwise, the XRD pattern of M-G should have some peaks from melamine itself. A (100) peak of M-G at 14.50° was indexed and represents tristriazine unit in-plane structural packing. The (100) indicates the hole-to-hole distance (d = 0.675 nm) in the nitride pores.[44]

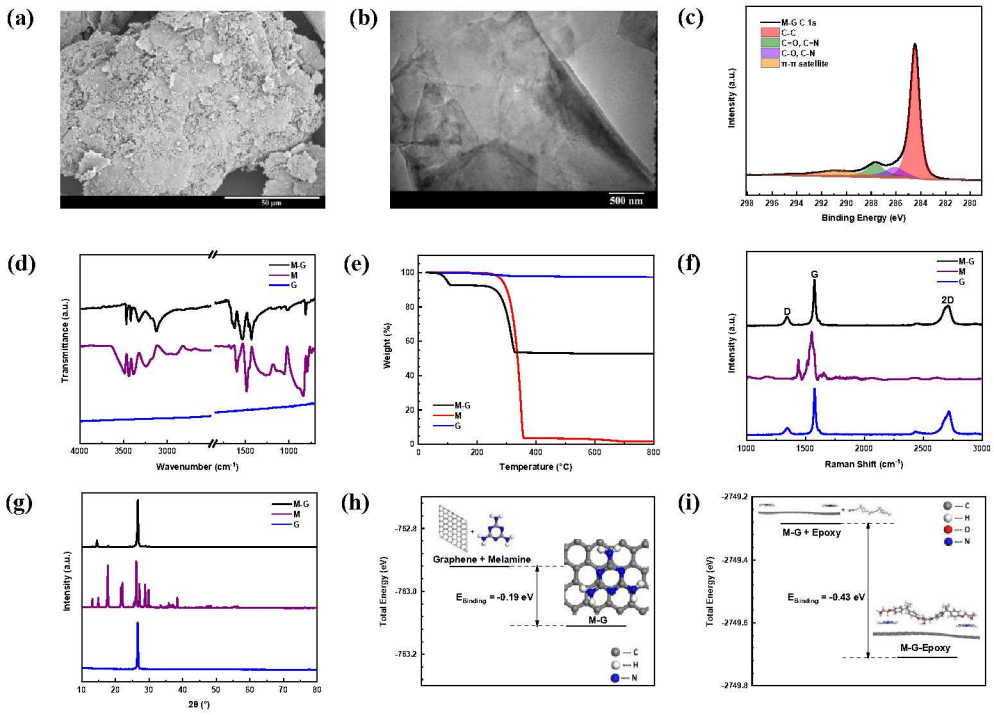

Figure 2. (a) SEM image and (b) TEM image of M-G. (c) XPS spectra of M-G in C 1s. The comparison of (d) FTIR, (e) TGA curves, (f) Raman spectra and (g) XRD pattern between G, M and M-G. (h) Energy of the graphene, melamine, and the M-G structures and (i) energy of the M-G, epoxy, and M-G-epoxy structures from DFT calculation. The energy difference within each figure indicates the binding energy.

To further fundamentally investigate the connection between melamine and graphene, density functional theory (DFT) has been employed with the Vienna Ab Initio Simulation Package (VASP). Melamine was relaxed on top of the infinite graphene surface, on which one melamine molecule adsorbed onto the graphene, consisting of 72 carbon atoms in the unit cell with a 20 Å vacuum perpendicular to the graphene surface. To avoid the local minimum issue during the relaxation simulation, different distances between graphene and melamine (from 1.1 Å up to 2.0 Å) and different adsorption spots with respect to graphene were considered in the initial

configurations. The optimized M-G configuration, shown in figure 2h, with a 3.7 Å distance between graphene and melamine indicates a -0.19 eV binding energy. This negative binding energy confirms the interaction between graphene and melamine posited by the experiments and is consistent with previous studies with the M-G system.[45,46] Additionally, the interaction between M-G and epoxy also has been demonstrated by DFT. One epoxy molecule was added on top of the M-G configuration, reacting with the amine groups of 2 melamine molecules on top of a 3×1×1 graphene supercell (216 carbon atoms). More information about the model is given in the support information. The simulation results in Figure 2i demonstrate that the binding energy between one epoxy molecule and two melamine molecules is -0.43 eV, which further verifies the strong binding between epoxy and melamine.

2.2 Dynamic mechanical properties of melamine-graphene epoxy nanocomposite:

Thermal stability of the nanocomposite is essential because a high T_g and modulus can maintain the electric contact and characteristics of optimal DAFs.[47] For some commercial and military applications, they require a high T_g above 150 °C. 125 °C, the maximum operating temperature for conventional silicon dies, is lower than the recommended T_g for commercial and military applications.[48] Typically, epoxy-based DAFs can withstand long-term usage in the range of 125-150 °C; however, this temperature range needs to be improved to satisfy the requirements of high-power environments.[47] Moreover, industry applications demand a comparable lower curing temperature and faster curing schedule. As shown in Figure 3a-b, different ratios of

bisA and cresol novolac epoxy were fabricated and their network formation was investigated by dynamic mechanical analysis (DMA). With the ratio of bisA to cresol novolac epoxy decreasing, the storage modulus and T_g of epoxy resins both increase. The ratio of 5:5 (bisA to cresol novolac) achieved the largest storage modulus of 1169 MPa and the highest T_g of 161°C because most of the epoxide groups reacted and hence underwent ring-opening to produce a higher cross-link density than others.

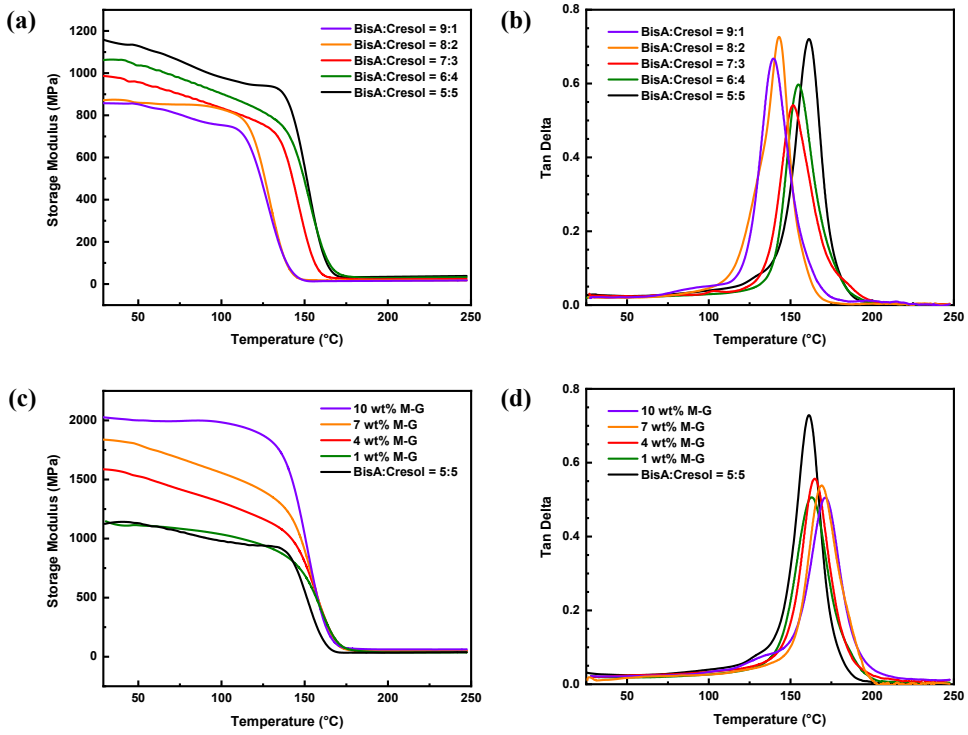

Figure 3. (a) Storage moduli and (b) loss factor between different ratios of Bis A to cresol novolac epoxy resins. (c) Storage moduli and (d) loss factor of different wt% loadings of M-G epoxy nanocomposites (neat epoxy is 0 wt%).

A more fundamental estimation of cross-link density was calculated by the following equation in the epoxy's rubbery region:[49,50]

$$X = \frac{E'}{3RT'}$$

Where X is the estimated cross-link density, R is the ideal gas constant (R = 8.314 J/(mol·K), E′ is the storage modulus at T′, and T′ is 30 °C higher than T_g. With the ratio of bisA to cresol novolac epoxy decreasing, the calculated cross-link density is increased. The ratio of 5:5 obtained a cross-link density of 8.3×10^{-3} mol/cm^3, which is much higher than the cross-link density of the ratio of 9:1 (3.9×10^{-3} mol/cm^3).

With the addition of M-G into epoxy resins, the stiffness increase leads to an enhancement of the storage modulus. This stiffness change results from amine groups reacting with epoxide groups, causing the formation of covalent bonds. Subsequently, the mobility of epoxy chains is restricted, enhancing the storage modulus. The M-G epoxy nanocomposites have the highest storage modulus of 2032 MPa at 10 wt% loading as shown in Figure 3c. It was also found that the T_g for 10 wt% M-G epoxy nanocomposites was 172 °C, about 11 °C higher than neat epoxy in Figure 3d. Similar to the storage modulus increase a higher T_g results from better interfacial connection between M-G and epoxy resins. More importantly, the s-triazine rings in melamine provide high primary bond strengths and rigid polymer chains due to its molecular symmetry and aromaticity.[51–53] Thus, the synergistic functions of both the mechanical interlocking of epoxy chains and the aromatic triazine rings, introduced by melamine, lead to the increase of T_g for epoxy nanocomposites under a curing schedule of 155 °C for 90 mins without any post-cure, and the curing schedule is appropriate and reasonable for DAF applications. The effects of curing process parameters such as curing temperature, heating rate, and curing time can influence properties such as T_g,

viscosity, and thermal stress of epoxy composites, and they can be explored in future studies.

2.3 Thermal properties of melamine-graphene epoxy nanocomposite

The thermal conductivity of 1 wt% graphene and 1 wt% M-G epoxy nanocomposites were measured and are presented in Figure 4a. M-G epoxy nanocomposites exhibit the highest thermal conductivity of 0.49 W/mK, about 0.09 and 0.32 W/mK higher than graphene-epoxy composites and neat epoxy resins, respectively. The higher thermal conductivity of M-G epoxy nanocomposites is attributed to the improved interfacial connection and increased filler dispersion. The amine groups of melamine could open the epoxy rings through the addition reaction by nucleophilic substitutions. Then the amine groups will connect the methylene groups of epoxies, and the epoxy rings will be opened to form hydroxyl groups which still connect with another methylene groups of epoxies. Better interfacial connections and uniform dispersion of fillers result in a decreased thermal resistance between epoxy and fillers. Figure 4b shows the thermal conductivity of different filler loadings of M-G epoxy nanocomposites. The addition of fillers improved the thermal conductivity over neat epoxy, which has a thermal conductivity of 0.17 W/mK. The 10 wt% M-G epoxy nanocomposites have a thermal conductivity of 1.07 W/mK, 6.4 multiples higher than that of neat epoxy resins. These results all demonstrate that melamine functionalization reduces the interfacial thermal resistance and facilitates thermal transport within the epoxy composites.

To determine the main contribution to interfacial thermal resistance in epoxy nanocomposites, effective medium theory (EMT) was used to calculate the interfacial thermal resistance. Because of M-G being randomly dispersed in epoxy resins by stirring and sonication, EMT can effectively and reasonably predict thermal interfacial resistance values.[54] Moreover, compared to the Foygel model, EMT focuses more on filler-polymer thermal interfaces, which is more suitable for M-G epoxy nanocomposites.[55,56] The thermal conductivity (K) of M-G epoxy nanocomposites was obtained by the following equations:[57]

$$K = K_m \frac{3 + 2V_f\left(\frac{K_p - K_m}{K_m}\right)}{3 - V_f\left[(1-\alpha) - \frac{K_m}{K_p}\right]}$$

$$\alpha = \frac{R \times K_m}{d}$$

where K_m and K_p are the thermal conductivity of the epoxy and the thermal conductivity of the fillers, respectively; V_f represents the volume fraction of the fillers; d symbolizes the thickness of the fillers; and R corresponds to the thermal interfacial resistance between epoxy and fillers. The Supporting Information contains the calculation details. For 1 wt% M-G epoxy nanocomposites, the calculated data of R is 5.12×10^{-3} m^2 K/W, which is lower than graphene-epoxy composites (6.54×10^{-3} m^2 K/W). In addition, 10 wt% M-G epoxy nanocomposites show even lower thermal interfacial resistance values of 2.56×10^{-3} m^2 K/W. These computed values concur with

the trend found from measuring the thermal conductivity of epoxy composites in Figure 4a-b.

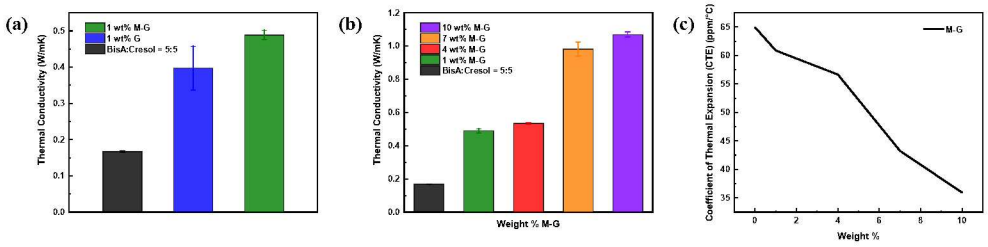

Figure 4. (a) A comparison of the thermal conductivities of neat epoxy, graphene epoxy nanocomposites and M-G epoxy nanocomposites at 1 wt% loading. (b) A comparison of the thermal conductivities of neat epoxy and M-G epoxy nanocomposites at different wt% loading. (c) The CTE of M-G at different wt% loading.

Along with thermal conductivity, another essential thermal property in epoxy composites, with regard to the reliability of DAF applications, is the CTE. The thermal stress will occur in the die bonding interface when the CTE mismatch of two materials are connected to DAFs by heat pressing. The thermal stress will remain at the interface to yield residual strain, which will cause die warpage and then result in package cracking.[58] In particular, for TSV 3D packaging, multiple-die stacking structures induce more serious thermal stress which can be detrimental to DAFs.[59] Typically, dies and copper substrates have an ultra-low CTE of 3 ppm/°C and 17 ppm/°C, respectively.[11] Therefore, DAFs are also expected to have a low CTE to connect die and substrate or die and die. As shown in Figure 4c, due to M-G enhancing the stiffness and improving the dimensional stability, an increase in filler loading led to a decrease in the CTE of epoxy nanocomposites. For 10 wt% M-G epoxy nanocomposites, the CTE was only

35.93 ppm/°C, about 29 ppm/°C lower than neat epoxy. This is because the M-G has connected with epoxy by covalent bonding, and the connection prevents volumetric contraction.[60] Moreover, graphene nanosheets naturally have a negative in-plane CTE. Thus, this property also contributes to the net reduction in the CTE of the composite.[61]

2.4 Moisture adsorption and electrical resistivity of melamine-graphene epoxy nanocomposite:

Moisture adsorption is also important for the reliability of DAFs because adsorbed moisture can be vaporized at high temperature processing, and this high-pressure water vapor causes the package cracking or interface delamination, commonly known as popcorn failure in semiconductor packaging.[62] Additionally, moisture acts as the plasticizer to reduce the modulus and T_g for the cured epoxy composites.[63] Thus, lower moisture adsorption of DAFs is demanded by semiconductor applications. The moisture adsorption behavior is plotted in Figure 5a under the 85 °C/85%RH conditions. All of samples were done through carful weight measurements before and after HAST test at the certain time. Neat epoxy resins have higher moisture adsorption than M-G epoxy nanocomposites because inorganic graphene fillers do not adsorb any moisture. Additionally, melamine modifications lead to less polymer chain movement and more cross-linking, constraining the rotation and alignment motions of polar groups of both melamine and epoxy. This reduces the overall polarity of the epoxy composite. However, melamine itself will give more amine polar groups on the surface of graphene. When the filler loading increase from 4 wt% to 7 wt%, these two competing factors are

nearly balanced out in their effect on moisture adsorption. However, with the filler loading continuing to increase, polar groups of melamine and epoxy have been further influenced and constrained because more amine groups react with epoxy to form the covalent bonds.

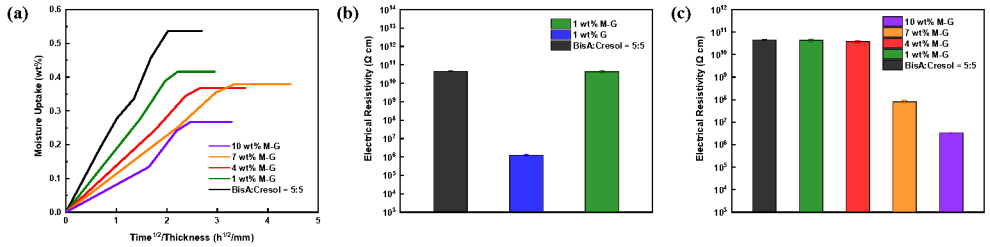

Figure 5. (a) The comparison of moisture adsorption between neat epoxy and M-G epoxy nanocomposites at different wt% loading. (b) The comparison of electric resistivity between neat epoxy, graphene, and M-G epoxy nanocomposites at 1 wt% loading. (c) The electrical resistivity of M-G epoxy nanocomposites at various wt% loading.

Electrical insulation is another essential factor for DAFs because highly thermally conductive and electrically insulating epoxy nanocomposites are desired for TSV multi-die stacking structures to prevent short circuiting. In Figure 5b, 1 wt% M-G showed an electrical resistivity of 4.26×10^{10} Ω cm, more than an order of magnitude greater than the resistivity of common semiconductors (10^9 Ω·cm).[64] Moreover, it presented a 10^4 times larger electrical resistivity than 1 wt% G (1.24×10^6 Ω cm) due to the insulating melamine coating layers. Although the electric resistivity is decreasing with increasing M-G loading, because more M-G fillers connect to form an electrically conductive network, 10 wt% M-G epoxy composites still has an electrical resistivity of 3.31×10^6 Ω cm, as shown in Figure 5c. This value is still higher than that of 1 wt% G epoxy

composites.

2.5 Performance test and simulations of the epoxy nanocomposites in DAFs application:

Towards investigating the heat dissipation ability of epoxy nanocomposites as DAFs in practical applications, a test design was constructed to monitor the cooling ability of electronic devices. A schematic of this configuration is shown in Figure 6a – a stack-up of dies with intermediate DAFs, attached to a ceramic heater and a copper heatsink. Epoxy nanocomposites as DAFs were placed between each of the die-die interfaces, as well as in between the die-copper interface. In total, there were three stacked dies with three layers of DAF. These dies were obtained from Intel, and they all have the same geometry (36.97 mm^2). In this system, the primary heat source is a ceramic heater that is powered by a tunable power supply. A cycling water pump contacts the thermally conductive copper heat sink to allow heat to dissipate as it is generated. This occurs in the bottommost level of the stacked setup. Performance tests were run at ambient room temperature (25°C), and an infrared camera was directed at the top layer of the stackup to measure temperature. During the operation process, M-G epoxy nanocomposites exhibited slower temperature rises and lower equilibrium temperatures under a power of 15 W compared to neat epoxy, as shown in Figure 6b. Equilibrium temperature for the 10 wt% M-G epoxy nanocomposites was around 176°C at steady state in 870 s, as also observed by the IR camera, a temperature value which was 21°C lower than neat epoxy. Equilibrium temperatures (Figure 6c and S3a-

g) of the ceramic heater relative to the applied power is plotted in Figure 6d for both neat epoxy and 10 wt% M-G epoxy nanocomposites. In comparison of their respective slope values, 10.6°C/W (epoxy) and 9.4°C/W (M-G), it was demonstrated that the M-G epoxy composites reached an 11.3% increase in cooling efficiency over neat epoxy. In all, the performance tests support that M-G epoxy nanocomposites have improved heat dissipation as DAFs in real operations of electronic encapsulation, consistent with their superior thermal conductivities.

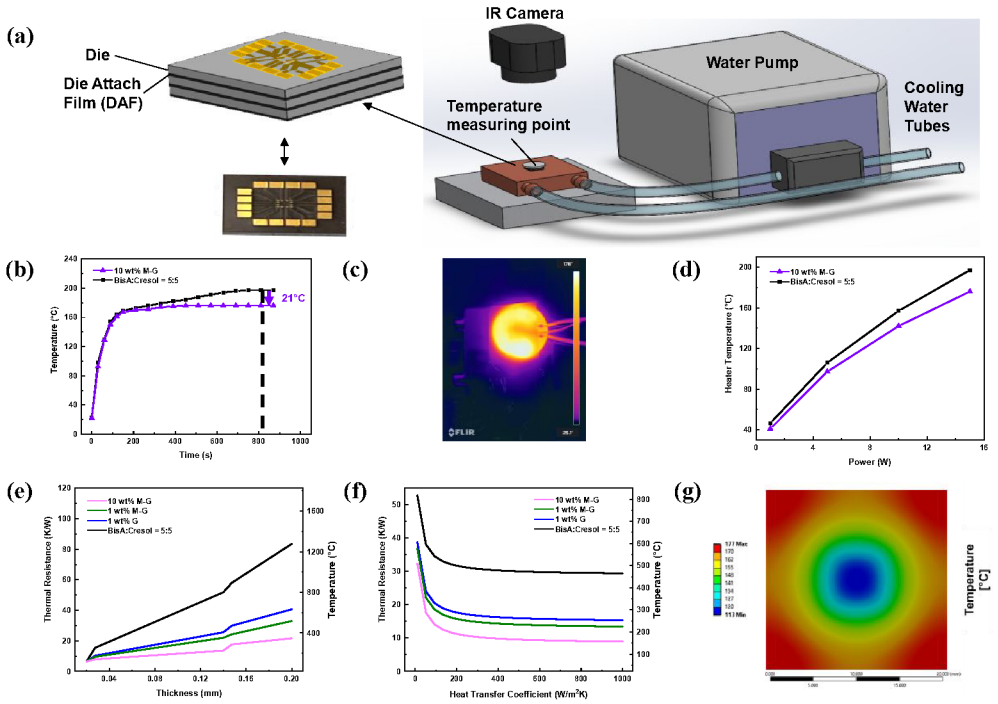

Figure 6. (a) An illustration of the DAFs evaluation setup. (b) The time-dependent temperature of the ceramic heater at 15 W power reaching the steady state. (c) A circular ceramic heater at a power of 15 W under an IR camera for 10 wt% M-G epoxy nanocomposites as DAFs. (d) The temperature of the ceramic heater with different applied powers. (e) The junction thermal resistance and temperature of DAFs as a function of thickness. (f) The junction thermal resistance and temperature of DAFs as a

function of the heat transfer coefficient. (g) The modeling ceramic heater temperature of 10 wt% M-G epoxy nanocomposites as DAFs at power of 15W.

Through finite element analysis (FEM), it is possible to further understand the behavior of these epoxy nanocomposite as DAFs – gaining new insights into their development and optimization for more reliable and robust performance. In order to thoroughly capture the capabilities of DAFs in actual applications for thermal management, a parametric study was carried out in ANSYS. More information about the FEM modeling can be found in the supporting information. For direct comparison to the performance test setup, boundary and loading conditions for this stackup were close representations – an applied power of 15 W as losses from the heat generating source, and an applied heat transfer coefficient of 300 W/m^2K at the copper heatsink. It was found that the simulated temperatures were in reasonable agreement with the experimental temperatures. From Figure 6e-g and S4a-c, the 10 wt% M-G epoxy nanocomposite DAFs had noticeably lower maximum junction temperature (176.68°C) and junction-to-ambient thermal resistance (10.31 K/W) in comparison to the other DAFs. These increasingly lower temperatures represent the effectiveness of the modifications of epoxy nanocomposite DAFs for thermal management. With each successive complexity added to the DAFs, from neat epoxy to M-G epoxy nanocomposites, overall improvements were observed.

In addition, several variables were taken into consideration in this time-based modeling study to create an in-depth review of their effects. Geometric properties were

varied, including the thickness of the DAF layers (20 - 200 µm). Material selection was also varied, including the type of DAF, highlighting the differences in thermal conductivities and specific heat capacities across the materials. Different types of cooling solutions were also considered – ranging from low air cooling at 10 W/m^{2}K to forced air cooling at 100 W/m^{2}K up to intensive liquid cooling above 1,000 W/m^{2}K. From the parametric modeling study (Figure 7a-b and S4d-e), response surface images reveal the relationships between different variables. Comparing the response of two variables is useful in determining their relative effect. Altogether, M-G epoxy nanocomposite DAFs are more effective for thermal management, as evidenced by lower temperatures and lower thermal resistances. Additionally, they can maintain these lower temperatures at lower heat transfer coefficients, such that simpler cooling solutions would be possible to maintain operation.

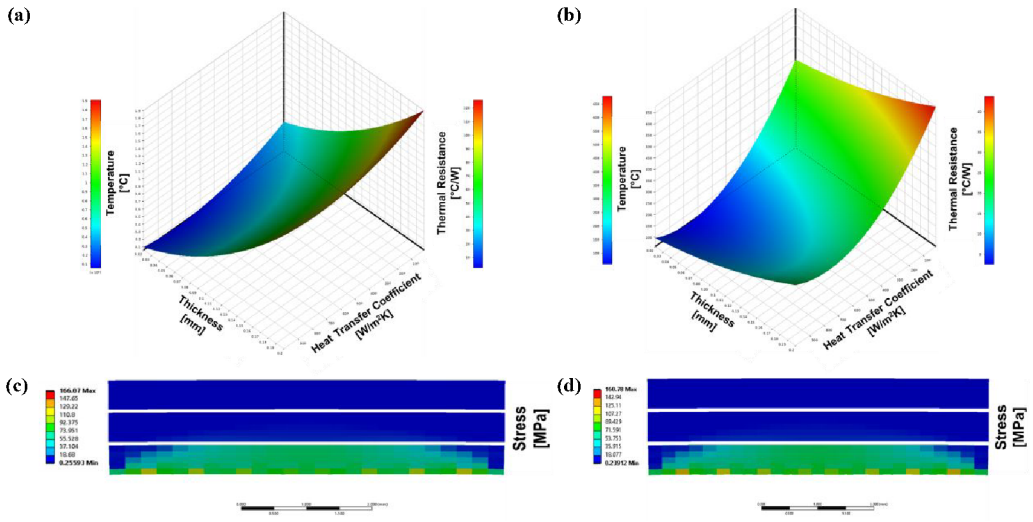

Figure 7. The 3D response picture of (a) neat epoxy and (b) 10 wt% M-G epoxy nanocomposites for changes in temperature and thermal resistance with respect to thickness and heat transfer coefficient. Three dies in the configuration system for (c) neat epoxy as DAFs and (d) 10 wt% M-G epoxy

nanocomposites as DAFs have their thermal stresses modeled.

Furthermore, through finite element analysis, the thermomechanical behavior of these stack-ups were also compared. Such aspects are important in that due to the variations in storage moduli and CTE among the different types of DAFs, there can be substantial differences. Especially as die-stacking has become more prominent, it has become important to consider these implications. As seen in the stress distributions for the dies (Figure 7c-d and S4f), the 10 wt% M-G epoxy nanocomposite as DAFs had lower maximum and average stresses of 160.78 MPa and 30.40 MPa in the dies due to less CTE mismatches. In terms of thermal stresses on the dies, trade-offs can be seen as in the M-G loading. At higher loadings – moduli increase as CTE decreases. These lower coefficients contribute toward less stresses from CTE mismatches between the die attach films and the dies themselves, but higher moduli can also contribute toward more stress as the films are less compliant. However, with a 77% increase in modulus and a 41% decrease in CTE from 1 wt % to 10 wt% in M-G, there was an overall 3% decrease in maximum stress and 1% decrease in average stress for the dies. There was a smaller percentage decrease in CTE as compared to modulus, yet it still resulted in decreases in stresses. Therefore, this demonstrates that CTE is more impactful on stresses than modulus. Furthermore, there was an increase in thermal conductivity by 121% from 1 wt % to 10 wt% loading in M-G. This higher thermal conductivity also contributes to lesser stresses due to more gradual temperature gradients throughout the bodies in the stackup. It is important to recognize that these material properties are closely intertwined and, together, influence stresses.

3 Conclusions

In summary, melamine functionalized graphene epoxy nanocomposites have been fabricated through a non-destructive ball milling process, and their interfacial connections have been studied through both experimental and simulated methods. The π−π stacking interaction makes graphene nanosheets present better dispersion without creating any defects on the surface. In addition, the aromatic triazine rings of melamine increase T_g to improve the thermal stability, and the amine groups of melamine react with epoxy to decrease the interfacial thermal resistance. M-G epoxy nanocomposites reached a high thermal conductivity of 1.08 W/mK at 10 wt% loading. This is 6.4 multiples higher than that of neat epoxy. Moreover, M-G epoxy nanocomposites exhibit superb thermal stability, an effective low CTE, low moisture adsorption, and a useful high electrical resistivity. Since M-G epoxy nanocomposites have exhibited an increased ability to cool the device and an increased ability to dissipate heat, as shown by experimentation and modeling, these modified nanocomposites pave a new pathway for DAFs in the future of electronic devices.

Supporting Information

Supporting Information is available from the RSC Publications or from the author.

Authors Contributions

Zhijian Sun: Experiments, Analysis, Writing, Review and Editing. **Ryan Wong**: Modeling and Data analysis. **Yifan Liu**: Modeling and Data analysis. **Michael Yu**:

Data Analysis and Editing. **Jiaxiong Li**: Data Analysis and Editing. **Daron Spence**: Characterization. **Mingyue Zhang**: Characterization. **Mohanalingam Kathaperumal**: Review and Editing. **Ching-Ping Wong**: Conceptualization and Funding acquisition.

Conflicts of interest

There are no conflicts to declare.

Acknowledgements

This work was supported by the Industry Consortium at the Georgia Tech Packaging Research Center (PRC). This work was performed in part at the Georgia Tech Institute for Electronics and Nanotechnology, a member of the National Nanotechnology Coordinated Infrastructure (NNCI), which is supported by the National Science Foundation (Grant ECCS-2025462).

References

1 Y. H. Jung, T.-H. Chang, H. Zhang, C. Yao, Q. Zheng, V. W. Yang, H. Mi, M. Kim, S. J. Cho, D.-W. Park, H. Jiang, J. Lee, Y. Qiu, W. Zhou, Z. Cai, S. Gong and Z. Ma, *Nat. Commun.*, 2015, **6**, 7170.

2 R. Geyer and V. Doctori Blass, *Int. J. Adv. Manuf. Technol.*, 2010, **47**, 515–525.

3 D. R. Frear, *JOM*, 1999, **51**, 22–27.

4 J. Watson and G. Castro, *J. Mater. Sci. Mater. Electron.*, 2015, **26**, 9226–9235.

5 *3D IC RF SiPs*, 2018, i–xxxv.

6 S. K. Pienimaa, J. Valtanen, R. Heikkila and E. Ristolainen, in *2001 Proceedings. 51st Electronic Components and Technology Conference (Cat. No.01CH37220)*, 2001, pp. 361–366.

7 C.-G. Hwang, in *2002 IEEE International Solid-State Circuits Conference. Digest of Technical Papers (Cat. No.02CH37315)*, 2002, vol. 1, pp. 24–27 vol.1.

8 H. Liao, M. Miao, X. Wan, Y. Jin, L. Zhao, B. Li, Y. Zhu and X. Sun, in *2008 9th International Conference on Solid-State and Integrated-Circuit Technology*, 2008, pp. 1199–1202.

9 G. Katti, M. Stucchi, K. De Meyer and W. Dehaene, *IEEE Trans. Electron Devices*, 2010, **57**, 256–262.

10 M. Motoyoshi, *Proc. IEEE*, 2009, **97**, 43–48.

11 D. Lu and C. P. Wong, *Materials for Advanced Packaging*, New York, NY : Springer US : Imprint: Springer, 2nd ed. 20., 2017.

12 Y. Li and C. P. Wong, *Mater. Sci. Eng. R Reports*, 2006, **51**, 1–35.

13 B. R. Mose, I.-S. Son and D.-K. Shin, *Microelectron. Reliab.*, 2018, **91**, 15–22.

14 J. Choi and S. J. An, *J. Electron. Mater.*, 2020, **49**, 4265–4271.

15 H. Liu, Q. Pan, S. Xu, J. Wang, L. Li and X. Wu, in *2021 22nd International Conference on Electronic Packaging Technology (ICEPT)*, 2021, pp. 1–5.

16 Q. Jia, G. Zou, H. Zhang, W. Wang, H. Ren, Z. A, Z. Deng, S. Yan, D. Shen and L. Liu, *Appl. Surf. Sci.*, 2021, **554**, 149579.

17 A. T. Cheung, in *56th Electronic Components and Technology Conference 2006*, 2006, p. 5 pp.

18 V. R. Manikam and K. Y. Cheong, *IEEE Trans. Components, Packag. Manuf. Technol.*, 2011, **1**, 457–478.

19 X. Mao, J. Liu, F. Yu, X. Fu, C. Hang, H. Chen and M. Li, *J. Mater. Sci. Mater. Electron.*, 2022, **33**, 5599–5612.

20 H.-P. Su, C.-C. Lee and A. Horng, in *2022 IEEE 72nd Electronic Components and Technology Conference (ECTC)*, 2022, pp. 2236–2243.

21 L. Yan, J. Yao, Y. Dai, S. Zhang, W. Bai, K. Gao, H. Yang and Y. Wang, *Electron.* , 2022, 11.

22 M.-C. Hsiao, C.-C. M. Ma, J.-C. Chiang, K.-K. Ho, T.-Y. Chou, X. Xie, C.-H. Tsai, L.-H. Chang and C.-K. Hsieh, *Nanoscale*, 2013, **5**, 5863–5871.

23 Z. Liu, Y. Chen, Y. Li, W. Dai, Q. Yan, F. E. Alam, S. Du, Z. Wang, K. Nishimura, N. Jiang, C.-T. Lin and J. Yu, *Nanoscale*, 2019, **11**, 17600–17606.

24 Z. Sun, J. Li, M. Zhang, M. Yu, K. Moon and C. Wong, in *2021 IEEE 71st Electronic Components and Technology Conference (ECTC)*, 2021, pp. 607–612.

25 A. A. Balandin, S. Ghosh, W. Bao, I. Calizo, D. Teweldebrhan, F. Miao and C.

N. Lau, *Nano Lett.*, 2008, **8**, 902–907.

26 Y. Zhang, Z. Wang, P. Yu, X. Yang, Z. Sun, Y. Zhang, Y. Wu and C. Jiang, *Compos. Sci. Technol.*, 2022, **226**, 109560.

27 G. Lian, C.-C. Tuan, L. Li, S. Jiao, Q. Wang, K.-S. Moon, D. Cui and C.-P. Wong, *Chem. Mater.*, 2016, **28**, 6096–6104.

28 S. Cui, W. Wu, C. Liu, Y. Wang, Q. Chen and X. Liu, *Nanoscale*, 2021, **13**, 18247–18255.

29 D. An, Z. Li, H. Chen, C. Liang, Z. Sun, J. Li, J. Yao, Y. Liu and C. Wong, *Compos. Part A Appl. Sci. Manuf.*, 2022, **156**, 106890.

30 Z. Sun, R. Wong, M. Yu, J. Li, M. Zhang, L. Mele, J. Hah, M. Kathaperumal and C.-P. Wong, *Chem. Eng. J.*, 2022, **439**, 135621.

31 L. P. Biró, P. Nemes-Incze and P. Lambin, *Nanoscale*, 2012, **4**, 1824–1839.

32 Y. Yao, X. Zeng, F. Wang, R. Sun, J. Xu and C.-P. Wong, *Chem. Mater.*, 2016, **28**, 1049–1057.

33 C. G. Robertson, C. J. Lin, M. Rackaitis and C. M. Roland, *Macromolecules*, 2008, **41**, 2727–2731.

34 Y. Sun, Z. Zhang, K. Moon and C. P. Wong, *J. Polym. Sci. Part B Polym. Phys.*, 2004, **42**, 3849–3858.

35 V. León, M. Quintana, M. A. Herrero, J. L. G. Fierro, A. de la Hoz, M. Prato and

E. Vázquez, *Chem. Commun.*, 2011, **47**, 10936–10938.

36 S. Kumar, G. Bouyssoux and F. Gaillard, *Surf. Interface Anal.*, 1990, **15**, 531–536.

37 M.-S. Lee, M. Park, H. Y. Kim and S.-J. Park, *Sci. Rep.*, 2016, **6**, 23224.

38 Y. Zhao, Z. Liu, W. Chu, L. Song, Z. Zhang, D. Yu, Y. Tian, S. Xie and L. Sun, *Adv. Mater.*, 2008, **20**, 1777–1781.

39 S. C. Yan, Z. S. Li and Z. G. Zou, *Langmuir*, 2009, **25**, 10397–10401.

40 R. S., S. P.N. and R. S., *Int. J. Hydrogen Energy*, 2016, **41**, 20779–20786.

41 D. Wei, Y. Liu, Y. Wang, H. Zhang, L. Huang and G. Yu, *Nano Lett.*, 2009, **9**, 1752–1758.

42 J. Cha, J. Kim, S. Ryu and S. H. Hong, *Compos. Part B Eng.*, 2019, **162**, 283–288.

43 Y. Yao, Z. Lin, Z. Li, X. Song, K.-S. Moon and C. Wong, *J. Mater. Chem.*, 2012, **22**, 13494–13499.

44 S. Martha, A. Nashim and K. M. Parida, *J. Mater. Chem. A*, 2013, **1**, 7816–7824.

45 V. León, A. M. Rodriguez, P. Prieto, M. Prato and E. Vázquez, *ACS Nano*, 2014, **8**, 563–571.

46 J. D. Wuest and A. Rochefort, *Chem. Commun.*, 2010, **46**, 2923–2925.

47 F. Lo, M. Leblon, R. Amigh and K. Chung, *Adhes. Sealants Ind.*, 2014.

48 K. Chano, G. M. Poliskie and J. Fregoso, *IEEE Trans. Components, Packag. Manuf. Technol.*, 2017, **7**, 217–220.

49 J.-S. Chen, C. K. Ober, M. D. Poliks, Y. Zhang, U. Wiesner and C. Cohen, *Polymer (Guildf).*, 2004, **45**, 1939–1950.

50 J. Li, C. Ren, Z. Sun, Y. Ren, H. Lee, K. Moon and C.-P. Wong, *ACS Appl. Mater. Interfaces*, 2021, **13**, 15551–15562.

51 P. E. Cassidy, *Thermally Stable Polymers, Synthesis and Properties*, Marcel Dekker, New York, 1980.

52 J.-K. Lin, Y. Yuki, H. Kunisada and S. Kondo, *J. Appl. Polym. Sci.*, 1990, **40**, 2113–2122.

53 P. Sojitra, K. Patel and H. Patel, *High Perform. Polym.*, 2010, **22**, 974.

54 J. Ma, T. Shang, L. Ren, Y. Yao, T. Zhang, J. Xie, B. Zhang, X. Zeng, R. Sun, J.-B. Xu and C.-P. Wong, *Chem. Eng. J.*, 2020, **380**, 122550.

55 D. An, X. Duan, S. Cheng, Z. Zhang, B. Yang, Q. Lian, J. Li, Z. Sun, Y. Liu and C.-P. Wong, *Compos. Part A Appl. Sci. Manuf.*, 2020, **135**, 105928.

56 D. An, S. Cheng, S. Xi, Z. Zhang, X. Duan, Y. Ren, J. Li, Z. Sun, Y. Liu and C.-P. Wong, *Chem. Eng. J.*, 2020, **383**, 123151.

57 C.-W. Nan, R. Birringer, D. R. Clarke and H. Gleiter, *J. Appl. Phys.*, 1997, **81**,

6692–6699.

58 C. Guan, M. Li, K. Chen, H. Chen and J. Wu, in *2012 14th International Conference on Electronic Materials and Packaging (EMAP)*, 2012, pp. 1–4.

59 J. Zhang, M. Todd and J. Huneke, in *Proceedings of the Sixth IEEE CPMT Conference on High Density Microsystem Design and Packaging and Component Failure Analysis (HDP '04)*, 2004, pp. 231–235.

60 W. Lin, K.-S. Moon and C. P. Wong, *Adv. Mater.*, 2009, **21**, 2421–2424.

61 D. Yoon, Y.-W. Son and H. Cheong, *Nano Lett.*, 2011, **11**, 3227–3231.

62 C. A. Harper, *Electronic Materials and Processes Handbook, Third Edition*, McGraw-Hill Education, New York, 3rd ed., 2004.

63 Y. He and X. Fan, *In-situ Characterization of Moisture Absorption and Desorption in a Thin BT Core Substrate*, 2007.

64 Y. Hu, C. Chen, Y. Wen, Z. Xue, X. Zhou, D. Shi, G.-H. Hu and X. Xie, *Compos. Sci. Technol.*, 2021, **209**, 108760.